INTERNATIONAL JOURNAL OF PRECISION ENGINEERING AND MANUFACTURING Vol. 17, No. 2, pp. 171-180 FEBRUARY 2016 / 171
DOI: 10.1007/s12541-016-0022-z ISSN 2234-7593 (Print) / ISSN 2005-4602 (Online)

Construction of Processing Maps based on Expanded Data by BP-ANN and Identification of Optimal Deforming Parameters for Ti-6Al-4V Alloy

Guo-zheng Quan[1,#], Hai-rong Wen[1], Jia-Pan[1], and Zhen-yu Zou[1]

1 State Key Laboratory of Mechanical Transmission, School of Material Science and Engineering, Chongqing University, Chongqing, 400044, China
Corresponding Author / E-mail: quangz3000@sina.com, TEL: +86-15922900904, FAX: +86-023-6511-1493

KEYWORDS: Back-propagation artificial neural network, Kinetic analysis, Processing maps, Ti-6Al-4V alloy

The intrinsic relationships between deforming parameters and microstructural mechanisms for Ti-6Al-4V alloy were analyzed by processing maps. A series of thermal compression tests were carried out in the temperatures range of 1023~1323 K (across β-transus) and strain rates range of 0.01~10 s^{-1} on a Gleeble-3500 thermo-mechanical simulator. Based on the stress-strain data collected from compression tests, a back-propagation artificial neural network (BP-ANN) model was developed, which presents reliable performance in tracking and predicting strain-stress data. By utilizing this model, the volume of stress-strain data was expanded. According to the intensive stress-strain data, the apparent activation energy was calculated to be 564.05 kJ mol^{-1} and 300.20 kJ mol^{-1} for α+β-phase field and single β-phase field, respectively. Moreover, the processing maps were constructed at finer intervals of temperature, from which, the stable regions with higher power dissipation efficiency ($\eta > 0.3$) and unstable regions with negative instability parameter ($\xi < 0$) were clarified clearly. By combining processing map with microstructure observations, two main stable softening mechanisms, i.e., globularization and dynamic recovery (DRV) were identified, and globularization-predominant ($0.3 < \eta < 0.55$) parameter domain ($\dot{\varepsilon} < 0.1\ s^{-1}$) in α+β-phase field and DRV-predominant ($0.25 < \eta < 0.41$) parameter domain ($0.032\ s^{-1} < \dot{\varepsilon} < 1\ s^{-1}$) in β-phase field were recommended.

Manuscript received: July 12, 2015 / Revised: November 8, 2015 / Accepted: November 11, 2015

1. Introduction

Ti-6Al-4V alloy, a typical $\alpha+\beta$ titanium alloy, has been extensively used in aerospace, energy and chemical processing industries because of its attractive specific strength, low density and great corrosion resistance etc. since its emergence in the early 1950s.[1-4] Generally, hot plastic processing in actual industrial processes such as hot forging or rolling is used for manufacturing required components with desired mechanical properties. It is known that the microstructure of a material determines its mechanical properties, and further influences service performance of the final products.[5,6] To achieve the desired mechanical properties, the desired microstructure of this alloy must be ensured. Therefore, the deeply understanding of microstructural evolution of this alloy is essential. On the other hand, the microstructure is extremely sensitive to process parameters such as deformation temperature, strain, strain rate, etc. Hence, it is valuable to deeply understand the relationships between microstructural evolution and process parameters for controlling and optimizing the mechanical properties of this alloy.

During hot plastic processing, the microstructural evolution of Ti-6Al-4V alloy is extremely complex due to the occurrence of $\alpha \rightarrow \beta$ phase transformation as well as the variation of morphology of α-phase. In the past years, great attentions have been paid to microstructural evolution and hot flow behaviors of Ti-6Al-4V alloy by various models. Ding et al.[7] described microstructural evolution of Ti-6Al-4V alloy under different hot working conditions using optical microscopy and scanning electron microscopy. Peng et al.[8] studied flow behaviors and deformation mechanisms of TC4-DT alloy with equiaxed $\alpha+\beta$ starting structure by measuring the true stress-strain curves, calculating the deformation active energy, establishing the kinetics equation and constructing its processing map at a true strain of 0.9 in a temperature range of 1203~1293 K and a strain rate range of 0.001~10 s^{-1}. Reddy et al.[9] described the effect of process parameters on the flow behaviors for Ti-6Al-4V alloy by using a developed artificial neural network model, which was successfully trained across different phase regimes ($\alpha+\beta$ to β-phase),

and further predicted the flow stress beyond experimental condition. Porntadawit et al.[10] investigated the deformation behaviors and microstructural evolution of Ti-6Al-4V alloy by establishing the constitutive models based on the hyperbolic sine equation. These models play a very important role in tracking the microstructural evolution as well as analyzing the effect of process parameters on microstructure. Among these, "processing map on the basis of dynamic materials model (DMM)" is considered as a powerful tool for controlling microstructural evolution and optimizing the hot forming process of an alloy, with which the flow instability regions and recommended processing domains can be clarified clearly. In the practical hot working process, this tool is used to design process parameters, which effectively eliminates the iteration work for process design.

In recent years, significant efforts have been made to investigate hot deformation behaviors and microstructural evolution of Ti-6Al-4V alloy by processing map. Park et al.[11] constructed the processing map of Ti-6Al-4V alloy by using the stress-strain data from compression tests in the temperature range of 1123~1273 K and strain rate range of 0.001~10 s^{-1}. Seshacharyulu et al.[12] studied microstructural mechanisms by constructing the processing map in the temperature range of 1023~1373 K and strain rate range of 0.0001~10 s^{-1}. From these works, it can be found that the stress-strain data is the foundation for calculating processing maps. Generally, these data were obtained from compressive or tensile tests. Nevertheless, due to the limitations of physical experiments, the volume of stress-strain data is relatively smaller. To construct accurate processing map, the enough stress-strain data must be insured. Now, it is widely accepted that the artificial neural network (ANN) is a reliable and effective approach for tracking and predicting strain-stress data.[1,9] This model can not only accurately track non-linear experimental data, but also well predict the stress-strain data beyond experimental data.

Now, ANN has been applied to construct processing map. Reddy et al.[13] predicted flow stress by ANN model and constructed processing maps at different strain by utilizing the predicted flow stress at finer intervals of strain rates and temperatures. Sun et al.[14] developed the processing map of Ti40 alloy by using the flow stress predicted by ANN model at the strain of 0.4. Wen et al.[15] constructed the processing maps of Ti-6Al-4V alloy based on the experimental stress-strain data and predicted stress-strain data respectively and then compared theoretical processing maps with experimental maps. It can be seen that constructing the processing maps with the predicted data by artificial neural network model is feasible. However, the comprehensive analysis of microstructural evolution for Ti-6Al-4V alloy by combining artificial neural network model with processing map is still scarce. In the present investigation, a back-propagation artificial neural network model was developed to expand stress-strain data of Ti-6V-4Al alloy at different conditions. Based on expanded strain-stress data, not only the processing maps at different strain but also constitutive equation at the strain of 0.5 was developed to accurately understand microstructural evolution of Ti-6Al-4V alloy.

In this paper, the strain-stress data of Ti-6V-4Al alloy were collected from a series of hot compressions in a wide temperature range of 1023~1323 K across β-transus and a large strain rate range of 0.01~10 s^{-1} with a height reduction of 60%. The volume of strain-stress data was expanded by a back-propagation artificial neural network model (BP-ANN). According to the intensive stress-strain data, the processing maps at true strains of 0.3, 0.5, 0.7 and 0.9 were constructed, meanwhile, the deformation active energy at a strain of 0.5 was calculated, and the kinetics equation was established for the α+β-phase field and the single β-phase field, respectively. From these processing maps, the stable and unstable parameter domains during hot compressions were clarified, in further, the deformation mechanisms such as globularization of α-phase mechanism predominant in α+β-phase and DRV of β-phase mechanism predominant in single β-phase were identified. The microstructural observation was conducted on the tested specimens to deeply understand the intrinsic relationships between the microstructures and processing parameters. The present work is of great guiding significance in practical application for designing and optimizing process parameters to obtain final products with desirable microstructures and desirable mechanical properties during hot plastic deformation.

2. Acquisition of Intensive Stress-Strain Data

2.1 Stress-strain data collection from experiments

The chemical compositions of Ti-6Al-4V alloy used in this work is as follows (wt.%): 6.50 Al, 4.25 V, 0.16 O, 0.04 Fe, 0.015 N, 0.02 C, 0.0018 H, and the balance of Ti. Its melting point is about 1903 K, and its β-transus is approximately 1263 K. The as-received material is an extruded billet with a diameter of 200 mm and a height of 50 mm. In order to eliminate the microstructural characteristics of deformed material, the extruded billet was annealed at 1123 K for 1.5 hour followed by air cooling. From this billet material total twenty-nine cylindrical specimens with a diameter of 10 mm and a height of 12 mm were machined by wire-electrode cutting. The twenty-eight ones of them correspond to the compression test schedule of different seven temperatures (1023 K, 1073 K, 1123 K, 1173 K, 1223 K, 1273 K and 1323 K) and different four strain rates (0.01 s^{-1}, 0.1 s^{-1}, 1 s^{-1} and 10 s^{-1}), while the left one is considered as the as-received specimen for the observation of original microstructure. In the compression tests, a fully integrated digital closed loop control thermal and mechanical testing system produced by DSI, Gleeble 3500, was adopted. This machine typically has a high speed heating system, a servo hydraulic system and a computer control and data acquisition system. Before a compression, by a unit of electro-spark overlaying welding on this machine, two K-type thermocouple wires with a diameter of 0.254 mm, i.e. two dissimilar conductors were welded on two spots with a distance of 1 mm at the mid-span of each billet where a temperature differential is experienced by the two different conductors. In the following, this specimen was fixed between the anvils exactly at the center without any deviation such that the deformation axis is straight avoiding the formation of irregular shape. Next, this specimen was resistance heated at a heating rate of 10 K/s and held for 180 s by thermo-coupled-feedback-controlled AC current, aiming to obtain a uniform temperature field and decrease the material anisotropy. Then this specimen was compressed with a fix height reduction of 60% under a constant temperature and a constant strain rate. After the compression, the deformed specimen was rapidly quenched in water to retain the deformed microstructure at high temperature. Such twenty-eight compression tests corresponding to seven temperatures and four strain rates were performed.

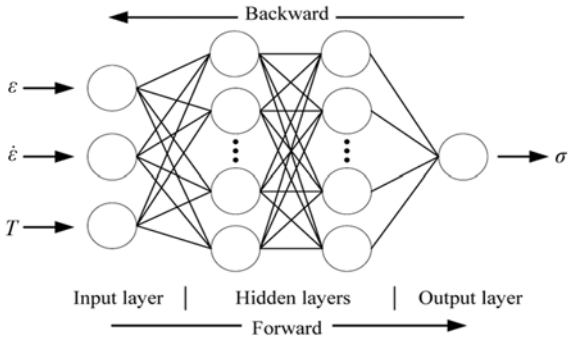

Fig. 1 The schematic drawing of the BP-ANN model

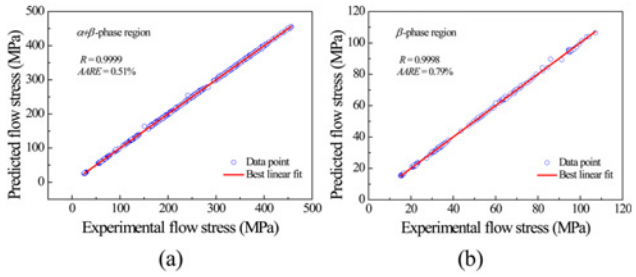

Fig. 2 Evaluation of the performance of the developed BP-ANN model by the comparison between the experimental and predicted flow stress data: (a) in α+β-phase temperature range; (b) β-phase temperature range

During these compression processes, the variations of nominal stress and nominal strain were monitored continuously by a personal computer equipped with an automatic data acquisition system. The true stress and true strain were derived from the nominal data according to the following formula: $\sigma_r = \sigma_N(1+\varepsilon_N)$, $\varepsilon_r = \ln(1+\varepsilon_N)$, where σ_r is the true stress, σ_N is the nominal stress, ε_r is the true strain and ε_N is the nominal strain.

2.2 Stress-strain data volume expansion by BP-ANN

In the past few decades, a large number of researchers have paid attention to developing various models to describe the effect of process parameters on flow stress.[16,17] It is widely accepted that ANN is an effective approach for complex and nonlinear systems such as the characterization of hot flow behaviors. Particularly, it has a good capacity to model the complex hot flow behaviors of titanium alloys.[1,18] A typical ANN consists of an input layer, an output layer and one or more hidden layers, and these layers are connected by the units called artificial neurons. The input layer receives outside signals, and the output layer generates output signals, and the hidden layer acts as a complex network architecture to simulate the complex nonlinear relationships between outside signals and output signals.[5] In this work, the training of ANN is undertaken using the back-propagation (BP) algorithm. BP algorithm is a typical means of adjusting the weights and biases by utilizing gradient descent to minimize the target error, and has a great representational power for dealing with highly nonlinear and strongly coupled relationship.[1,5]

In this investigation, the input variables of BP-ANN model include strain, strain rate and temperature, and the output variable is flow stress. Fig. 1 shows the schematic drawing of this BP-ANN model. The training of this model utilizes MATLAB, before which, a total of 2408 data sets were selected from experimental stress-strain curves, among which 504 datasets at the true strain from 0.05 to 0.9 with an interval of 0.05 were used to test the performance of the developed BP-ANN model. The remaining 1904 datasets were used to train the network model. Before training, both input and output variables were normalized by Eq. (1) within the range of 0~1 in order to ensure each variable laying in the same magnitude.

$$x_n = 0.05 + 0.25 \times \frac{x - 0.95x_{min}}{1.05x_{max} - 0.95x_{min}} \tag{1}$$

where x_n is the normalized value of x, x is the original data (temperature, strain rate, strain), x_{max} and x_{min} are the maximum and minimum value of x respectively.

To develop an excellent BP-ANN model, the structural parameters involving hidden layer number, transfer function, training function and neuron number for each hidden layer, are of great significance, and here two hidden layers were adopted in the current investigation to ensure a high training accuracy, which were adopted in many literatures.[5,13] The selected transfer function is "tan sigmoid" for each hidden layer, and "pure linear" for output layer. Besides, the training function is "trainbr.". The neuron number for each hidden layer is often chosen by using trail-and-error method. The neuron number in the current investigation was adjusted continually (three, four, etc.) in each hidden layer. Further, the neuron number for each hidden layer is determined by the value of mean square error (*MSE*), which is expressed by Eq. (2):

$$MSE = \frac{1}{N}\sum_{i=1}^{N}(E_i - P_i)^2 \tag{2}$$

where E_i is the experimental flow stress value; P_i is the predicted flow stress value and N is the number of stress-strain samples. The *MSE*-values were calculated as the training works of BP-ANN models with different neuron numbers were accomplished. The results show *MSE*-value decreases to the minimum value when the neuron number in each hidden layer is 18, suggesting that the BP-ANN model with 18 neurons in each hidden layer exhibits optimal performance.

Two statistical indicators of correlation coefficient (R) as Eq. (3) and average absolute relative error (*AARE*) as Eq. (4) were employed to estimate the predictability of the developed BP-ANN model.

$$R = \frac{\Sigma_{i=1}^{N}(E_i - \overline{E})(P_i - \overline{P})}{\sqrt{\Sigma_{i=1}^{N}(E_i - \overline{E})^2 \Sigma_{i=1}^{N}(P_i - \overline{P})^2}} \tag{3}$$

$$AARE(\%) = \frac{1}{N}\sum_{i=1}^{N}\left|\frac{E_i - P_i}{E_i}\right| \times 100 \tag{4}$$

where E_i is the experimental flow stress value; P_i is the predicted flow stress value; $\overline{E}$ and $\overline{P}$ are the mean values of E and P respectively; N is the number of predicted flow stress values.

Fig. 2 shows the comparisons between the experimental and calculated flow stress values from the developed BP-ANN model. All the data points lie on the 45° straight line. It is seen that R-values in α+β-phase temperature range and β-phase temperature range are 0.9999

and 0.9998, respectively, and the relative *AARE*-values are respectively 0.51% and 0.79%. The higher *R*-value and lower *AAR*E-value show that all the predicted values are in a very good agreement with the experimental results.

According to the established BP-ANN model, the intensive stress data were predicted in the temperatures of 1048 K, 1098 K, 1148 K, 1198 K, 1248 K and 1298 K and at the strain rates of 0.01 s^{-1}, 0.1 s^{-1}, 1 s^{-1} and 10 s^{-1}, which were above the experiment schedule. With this, the volume of stress-strain data was expanded. The experimental and predicted stress-strain curves are illustrated in Fig. 3. The intensive stress-strain data contributes to the accuracy improvement in the following computations. From the intensive stress-strain data in Fig. 3, it is summarized that the flow behaviors show a noticeable dependence on deformation conditions including temperature, strain and strain rate. Generally, the stress level decreases with increasing temperature and decreasing strain rate. This is due to the fact that lower strain rate provides enough time for dislocation recovery, and higher temperature supports more energy for it. It is widely accepted that the evolution of flow behaviors indicates the intrinsic interactions between work hardening and softening mechanisms. There are two different types of flow stress evolution along with true strain in the studied temperature range, i.e., DRX softening type and DRV softening type. In α+β-phase temperature range, flow stress rapidly increases before the true strain of 0.1, which is caused by severe work hardening. Following which, flow stress increases slower and slower till a single peak value due to the onset and enhancement of DRX, and subsequently, flow stress decreases gradually to a steady value due to the onset of complete DRX. This kind of flow stress evolution attributes to DRX softening type. In β-phase temperature range, flow stress sharply increases to a certain value, and then keeps a steady state due to the onset and enhancement of DRV. This kind of flow stress evolution attributes to DRV softening type.

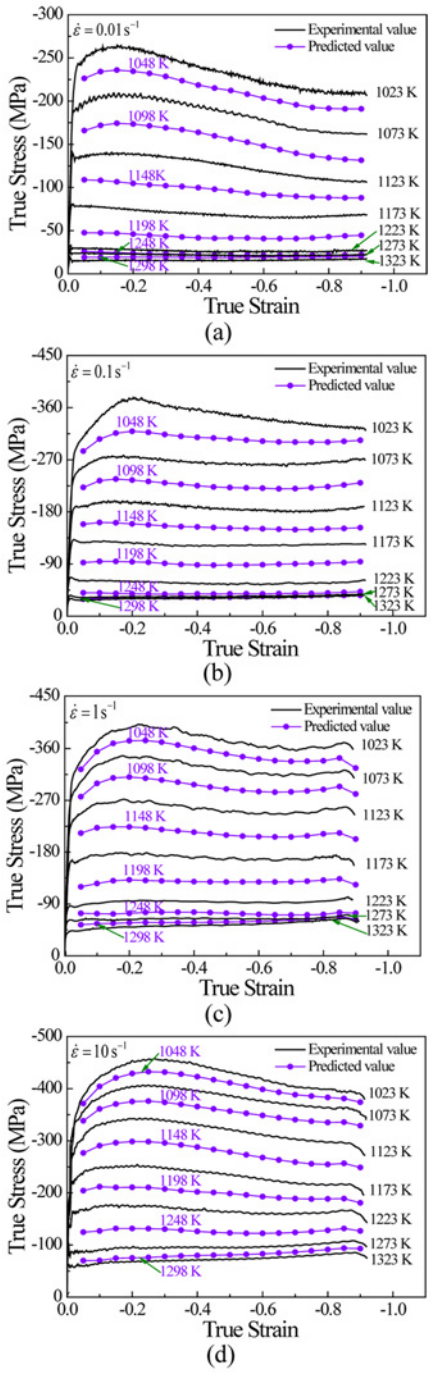

Fig. 3 The expanded stress-strain data of Ti-6Al-4V alloy under different temperatures and different strain rates (a) 0.01 s^{-1}, (b) 0.1 s^{-1}, (c) 1 s^{-1}, (d) 10 s^{-1}

3. Analytic Computation of the Intrinsic Relationships between Deforming Parameters and Microstructural Mechanisms

3.1 Kinetic analysis of microstructural mechanisms

In order to identify microstructural mechanisms of Ti-6Al-4V alloy in terms of kinetics, constitutive equations which relate the flow stress to strain rate and temperature should be developed. For the high temperature deformation, the Arrhenius-type equation is widely used to describe the relationship between the flow stress, temperature and strain rate, it can be expressed as:[1]

$$\dot{\varepsilon} = A(\sinh(\alpha\sigma))^n \exp\left(\frac{-Q}{RT}\right) \tag{5}$$

where $\dot{\varepsilon}$ is strain rate (s^{-1}); σ is flow stress (MPa); Q is activation energy of deformation ($kJmol^{-1}$); R is universal gas constant (8.314 $kJ\cdot K^{-1}\cdot mol^{-1}$); T is absolute temperature (K), n is stress exponent; A and α are the material constants. It is worth noting that n and Q are seen as important parameters since they indicate intrinsic microstructural mechanisms to some extent during hot deformation.

The intensive stress-strain data are employed to calculate the values of α, n, A and Q. The following are the evaluation procedures of material constants (α, n, A and Q) at a particular true strain of 0.5. The α+$\beta \rightarrow \beta$ transus for this grade of Ti-6Al-4V alloy is about 1263 K. Therefore the material constants (α, n, A and Q) would be calculated separately in α+β-phase region (under 1263 K) and single β-phase region (above 1263 K). Taking natural logarithm for both sides of Eq. (5), it can be expressed as:

$$\ln\dot{\varepsilon} = \ln A + n\ln(\sinh(\alpha\sigma)) - \frac{Q}{RT} \tag{6}$$

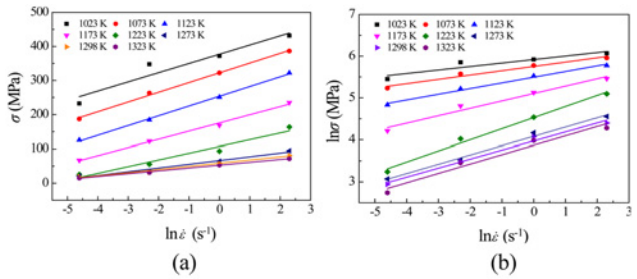

Fig. 4 Relationship between (a) σ and ln $\dot{\varepsilon}$, and (b) ln σ and ln $\dot{\varepsilon}$

When the deformation temperature (T) is a constant, the stress exponent (n) is defined as:

$$n = nR\frac{\partial \ln(\sinh(\alpha\sigma))}{\partial(1/T)}\bigg|_{\dot{\varepsilon}} \tag{7}$$

When the strain rate ($\dot{\varepsilon}$) is a constant, the activation energy (Q) is defined as:

$$Q = nR\frac{\partial \ln(\sinh(\alpha\sigma))}{\partial(1/T)}\bigg|_{\dot{\varepsilon}} \tag{8}$$

According to Eq. (7) and Eq. (8), the value of constant parameter α should be firstly calculated in order to determine the values of n and Q. The constant parameter α was obtained from the linear fitting of ln σ versus ln $\dot{\varepsilon}$ at low stress level and σ versus ln $\dot{\varepsilon}$ at high stress level[8] as shown in Fig. 4. Here, the value of α for α+β-phase region is 0.0061, and the one for single β-phase region is 0.0235 at the strain of 0.5.

Figs. 5 and 6 show the linear fitting of ln $\dot{\varepsilon}$ versus lnsinh($\alpha\sigma$) and 1000/T versus lnsinh($\alpha\sigma$) in different phase fields. The values of n and Q were obtained from the average slopes in Figs. 5 and 6. From Fig. 5, the values of n at the strain of 0.5 were calculated as 4.70 in α+β-phase field and 3.36 in β-phase filed respectively. Subsequently the values of Q at the strain of 0.5 were calculated as 564.05 kJmol^{-1} in α+β-phase field and 300.20 kJmol^{-1} in β-phase filed respectively. The obtained values for the activation energy are in good agreement with the results of Momeni et al..[19] During the hot deformation process, the deformation mechanism is closely associated with deformation activation energy. In the α+β-phase field, the value is much higher than that of self-diffusion in α-Ti (150 kJ·mol^{-1}) or in β-Ti (153 kJ·mol^{-1})[20] ruling out the possibility of diffusion being the rate controlling process, which is believed to induce the microstructural mechanism, i.e., globularization or dynamic recrystallization of lamellar α-phase. In the β-phase field, the activation energy is also higher than that of self-diffusion in β-Ti (153 kJ·mol^{-1}), which is believed to induce the microstructural mechanism, i.e., dynamic recovery.

It should be noted that Eq. (5) doesn't consider the comprehensive function of temperature and strain rate resulting the microstructural mechanism evolution. Continuing the analysis on the basis of the kinetic rate equation as Eq. (5), the temperature compensated strain rate parameter, i.e., Zener-Hollomon parameter, Z, given by Eq. (9) is evaluated on the basis of the above apparent activation energy.[8]

$$Z = \dot{\varepsilon}\exp\left(\frac{Q}{RT}\right) \tag{9}$$

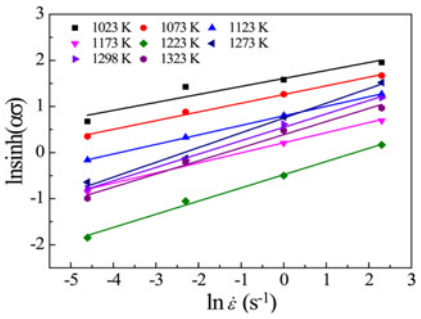

Fig. 5 Relationship between lnsinh($\alpha\sigma$) and ln $\dot{\varepsilon}$

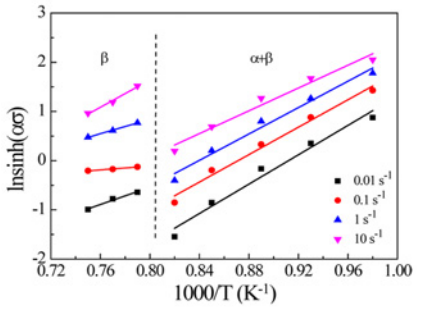

Fig. 6 Relationship between lnsinh($\alpha\sigma$) and 1000/T

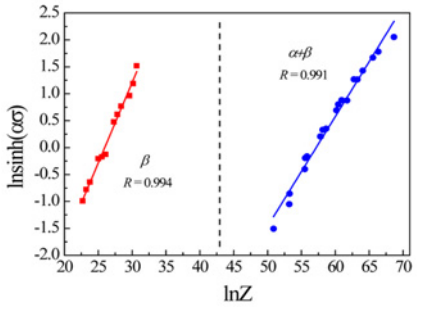

Fig. 7 Relationship between flow stress and Z parameter in α+β-phase and β-phase regions

According to Eqs. (5), (9) also can be rewritten as:

$$Z = \dot{\varepsilon}\exp\left(\frac{Q}{RT}\right) = A(\sinh(\alpha\sigma))^n \tag{10}$$

According to Eq. (10), the values of Z parameter were determined in α+β-phase region and β-phase region, and then plotted as a function of flow stress in Fig. 7. It is noted that there is a good linear correlation between flow stress and Z parameter. Flow stress increases with increasing Z parameter in the α+β-phase and the single β-phase fields.

3.2 Identification of microstructural mechanisms from processing maps

Processing map is a useful approach to optimize hot processing parameters and control microstructural evolution in metals and alloys.

It can be constructed based on the principle of dynamic materials model (DMM) proposed by Prasad Y. V. R. K. and Gegel H. L..[21-23] In DMM theory, the work-piece in the hot working process is considered as a nonlinear dissipator of power.[21,24] The total power (as Eq. (11)), P, absorbed by the work-piece is dissipated by the dissipator content, G, which is the power dissipated by plastic flow, and the dissipator co-content, J, which is the work related to metallurgical phenomenon such as dynamic recovery, dynamic recrystallization, phase transformation, etc.

$$P = \int_0^{\dot{\varepsilon}} \sigma d\dot{\varepsilon} + \int_0^{\sigma} \dot{\varepsilon} d\sigma = G + J \tag{11}$$

where σ is flow stress, and $\dot{\varepsilon}$ is strain rate. The partitioning of total power, P, between J and G is decided by strain rate sensitivity of flow stress (m) which is calculated by Eq. (12).

$$m = \frac{dJ}{dG} = \frac{\dot{\varepsilon} d\sigma}{\sigma d\dot{\varepsilon}} = \frac{d \lg \sigma}{d \lg \dot{\varepsilon}} \tag{12}$$

At a given temperature and strain, the J co-content is determined as Eq. (13).

$$J = \frac{m}{m+1} \sigma \dot{\varepsilon} \tag{13}$$

For an ideal linear dissipator, m=1 and $J_{max} = \sigma\dot{\varepsilon}/2$. The value of J for a non-linear dissipator is normalized with that of an ideal liner dissipator, and thus a dimensionless parameter called efficiency of power dissipation (η) is obtained as Eq. (14).

$$\eta = \frac{J}{J_{max}} = \frac{2m}{m+1} \tag{14}$$

The values of parameter η correspond with various microstructural evolution mechanisms of deformed work-piece. The variation of η-values along with temperature and strain rate constitutes the power dissipation map that exhibits different parameter domains correlated with specific microstructural mechanisms. To identify flow instability regimes during large plastic flow, a continuum instability criteria as Eq. (15) based on the extremum principle of irreversible thermodynamics applied to large plastic flow was proposed by Kumar and Prasad.[25] Eq. (15) defines the onset of flow instability during the hot working process. The variation of ξ-values with temperature and strain rate constitutes the instability map, which presents instability regimes where ξ-values is negative. Eventually, the processing map is obtained by superimposing the instability map over the power dissipation map. The processing map is used to provide optimum deformation parameters as well as describe the regimes of flow instability such as wedge cracking or flow localization.[26,27]

$$\xi(\dot{\varepsilon}) = \frac{\partial \lg(m/(m+1))}{\partial \lg \dot{\varepsilon}} + m < 0 \tag{15}$$

where $\xi(\dot{\varepsilon})$ is a dimensionless parameter.

Based on the intensive stress-strain data consisting of experimental data and predicted data by BP-ANN model, the processing maps of Ti-6Al-4V alloy at the strains of 0.3, 0.5, 0.7 and 0.9 were constructed as Fig. 8(a)~(d). In these processing maps, the stable and instable regimes were clarified clearly. In the processing map, the efficiency of power dissipation (η) is viewed as microstructural "trajectories", since it characterizes the rate of microstructural evolution and represents the

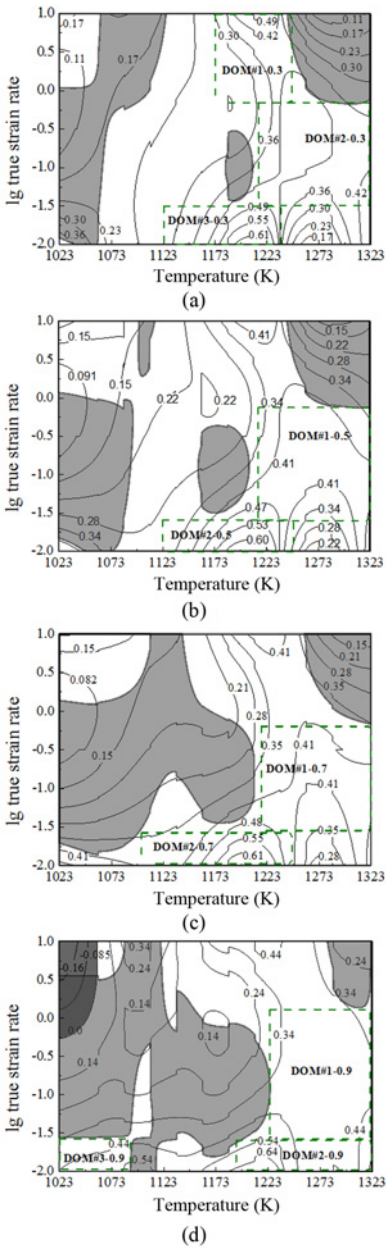

Fig. 8 The processing maps at true strain of (a) ε = 0.3, (b) ε = 0.5, (c) ε = 0.7, (d) ε = 0.9

dynamic microstructure state of the deformed material during the hot working process.[24] For titanium alloy, the η-value related to DRV is about 0.25, and the η-value corresponding to DRX or globularization is about 0.25~0.55. It is noted that superplasticity may occur when the η-value exceeds 0.55.[28] The processing map reveals the deterministic domains where the specific microstructural mechanisms occur. Generally, the dynamic restoration mechanisms in the stable domain include DRV, DRX, globularization and superplasticity. However, in the unstable domain there are several micro defects of instability including adiabatic shear bands, flow localization, dynamic strain aging, twinning, etc. By avoiding the regimes of flow instability and recommending the stable domains of proper microstructural mechanisms, the intrinsic workability of the material may be optimized, and microstructural control may be achieved.

From Fig. 8 (a)~(d), it can be seen that the distribution of efficiency exhibits similar features at the strains of 0.3, 0.5, 0.7 and 0.9, and it is worth noting that near β-transus, the iso-efficiency contours exhibit sharp demarcation at each map. This phenomenon is generally observed in some materials, in which phase transformation including precipitate dissolution occurs.[20] While instability regions show great change with increasing in strain from 0.3 to 0.9. Comparing the four maps with each other, it can be summarized that the instability flow occurs mainly in two regions for all strain, one locates in the lower temperature (1023~1073 K) and lower strain rate (0.032 s^{-1}), and the other locates in the higher temperature (1273~1323 K) and higher strain rate (1~10 s^{-1}). The former is caused by adiabatic shear bands or flow localization and the latter may be attributed to intercrystalline cracking. However, in the temperature range of 1123~1223 K and the strain rate range of 0.032~1 s^{-1}, the area of instability regions increases with increasing strain. According to the processing maps, the optimum deformation temperature range and strain rate range were obtained at strain 0.3, 0.5, 0.7 and 0.9, and they were marked by using thick line in each processing map. In Fig. 8(a), the map exhibits three domains with higher η-value (> 0.3): Domain #1-0.3 occurs in the temperature range from 1173 to 1248 K and strain rate range from 0.56 to 10 s^{-1}, with a peak η-value of about 0.49. Domain #2-0.3 occurs in the temperature range from 1213 to 1323 K and strain rate range from 0.032 to 0.56 s^{-1}, with a peak η-value of about 0.42. Domain #3-0.3 occurs in the temperature range from 1123 to 1248 K and strain rate range from 0.01 to 0.032 s^{-1}, with a peak η-value of about 0.61. In Fig. 8(b), the map exhibits two domains with higher η-value (> 0.3): Domain #1-0.5 occurs in the temperature range from 1213 to 1323 K and strain rate range from 0.032 to 1 s^{-1}, with a peak η-value of about 0.41. Domain #2-0.5 occurs in the temperature range from 1123 to 1248 K and strain rate range from 0.01 to 0.032 s^{-1}, with a peak η-value of about 0.60. In Fig. 8(c), the map exhibits two domain with higher η-value (> 0.3): Domain #1-0.7 occurs in the temperature range from 1223 to 1323 K and strain rate range from 0.032 to 1 s^{-1}, with a peak η-value of about 0.41. Domain #2-0.7 occurs in the temperature range from 1098 to 1248 K and strain rate range from 0.01 to 0.032 s^{-1}, with a peak η-value of about 0.61. In Fig. 8(d), the map exhibits three domains with higher η-value (> 0.3): Domain #1-0.9 occurs in the temperature range from 1223 to 1323 K and strain rate range from 0.032 to 1 s^{-1}, with a peak η-value of about 0.44. Domain #2-0.9 occurs in the temperature range from 1198 to 1323 K and strain rate range from 0.01 to 0.032 s^{-1}, with a peak η-value of about 0.64. Domain #3-0.9 occurs in the temperature range from 1023 to 1090 K and strain rate range from 0.01 to 0.03 s^{-1}, with a peak η-value of about 0.44.

4. Deep Understanding the Intrinsic Relationships by Microstructure Observations

The typical microstructures of the Ti-6Al-4V alloy were observed by optical microscopy in order to verify the stable and instable parameter regions, and even deeply understand the intrinsic relationships between the microstructures and processing parameters. Fig. 9(a)~(f) show the microstructures under different strain rates and temperatures lying in the stable domains of processing maps. Fig. 9(a)~(b) show the microstructures at the same strain rate of 0.01 s^{-1}, while two different

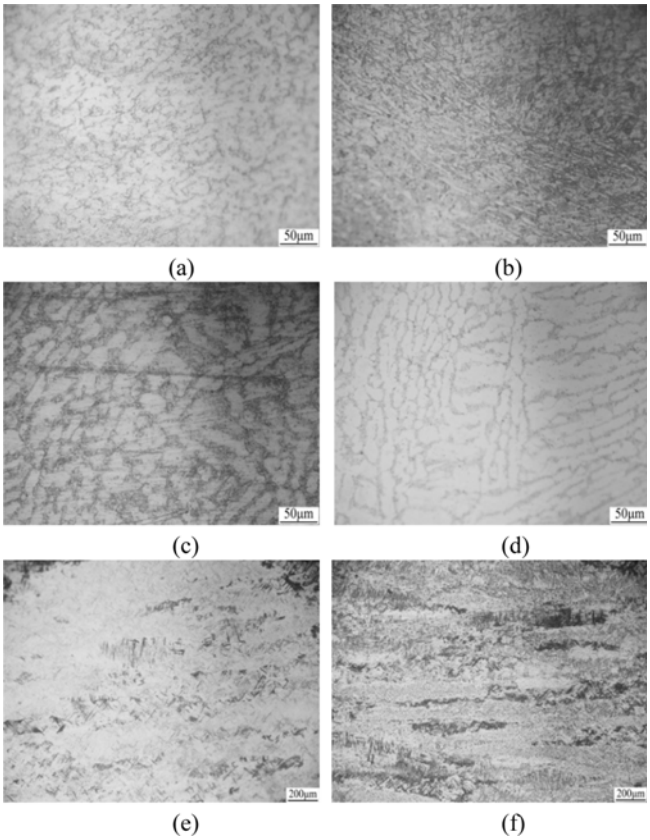

Fig. 9 The microstructures of the Ti-6Al-4V alloy in stable parameter region (a) 1023 K & 0.01 s^{-1}, (b) 1223 K & 0.01 s^{-1}, (c) 1173 K & 1 s^{-1}, (d) 1173 K & 10 s^{-1}, (e) 1323 K & 0.1 s^{-1}, (f) 1323 K & 1 s^{-1}

temperatures of 1023 K and 1223 K (under β transus). In Fig. 9(a) the microstructure under the stable deforming condition of 1023 K & 0.01 s^{-1} corresponding to a η-value of 0.44 shows that numerous equiaxed η-phase grains exist in β-matrix, which verifies the previous conclusion from processing map that globalization or DRX of η-phase is dominant when η-value is about 0.25-0.55. In Fig. 9(b) the microstructure under the stable deforming condition of 1223 K & 0.01 s^{-1} corresponding to a η-value of 0.64 shows that the refined and equiaxed α-phase grains disperse uniformly in β-matrix, which verifies the previous conclusion from processing map that superplasticity is dominant when η-value is above 0.55. For an α+β-titanium alloy, it is generally believed that fine grains and approximately equal volume fractions of η-phase and β-phase are beneficial to superplasticity because grain boundary sliding is easier to occur at higher temperature and lower strain rate.[29,30] By comparing the volume fractions of β-phase in Fig. 9(a) and 9(b), it was found that former is about 10%, and the later about 50%. Thus it can be concluded that the volume fraction of β-phase increases with increasing temperature before the β transus for this grade of Ti-6Al-4V alloy, here about 1263 K.

Fig. 9(c)~9(d) show the microstructures at the same temperature of 1173 K (under β transus), while two different strain rates of 1 s^{-1} and 10 s^{-1}. It was found that with decreasing strain rate, the volume fraction of β-phase as well as the proportion of equiaxed η-phase increases. Therefore, it can be deduced that the strain rate affects the $\alpha \rightarrow \beta$ phase transformation and globalization in some degree, in other word, the

amount of phase transformation and degree of globalization decrease with increasing strain rate due to insufficient time. It is always accepted that globularization process is desired deformation mechanism in α+β-phase field because it produces the desired fine equiaxed η-phase grains and good workability with high η-values.

Fig. 9(e)~9(f) show the microstructures in the single β-phase temperature range (above β transus). In Fig. 9(e) the microstructure under the stable deforming condition of 1323 K & 0.1 s^{-1} corresponding to a η-value of 0.4 shows that most of coarse β-phase grains are elongated, and only a few β-phase grains are broken with curved boundaries. In Fig. 9(f) the microstructure under the stable deforming condition of 1323 K & 1 s^{-1} corresponding to a η-value of 0.3 shows that all of coarse β-phase grains are elongated and the grain boundaries become straight. It can be summarized that at the temperatures above β transus, a lower strain rate makes the coarse β-phase grains refined in some degree by broken mechanism, but DRV of β-phase is always the dominant softening mechanism.

As mentioned previously, the flow instability regions have been identified in shade from the developed processing maps at a series of true strains. Fig. 10(a)~10(c) show the observed microstructures under different strain rates and temperatures lying in the instability parameter regions of processing map in Fig. 8(d). Fig. 8(d) corresponds to the final true strain of 0.9, i.e., the compression ending moment, shows the instability regions, in which the instable microstructural defects such as flow localization band and crack may occur. Fig. 10(a)~10(b) show the instable microstructures in the α+β-phase temperature range (under β transus). In Fig. 10(a) the microstructure under the unstable deforming condition of 1023 K & 1 s^{-1} shows that local flow phenomenon occurs at an angle of about 45° to the compressive axis. It is widely accepted that the adiabatic shear band as well as the low thermal conductivity of this alloy causes local flow, namely, the local heat produced during hot deformation is not conducted away in a relatively short time, and then it reduces the local flow stress and causes local flow.[12] It is noted that the intense local flow possibly results in cracking when these specimens deformed at lower temperatures and higher strain rates. In Fig. 10(b) the microstructure under the unstable deforming condition of 1173 K & 0.1 s^{-1} shows that cracking appears at the boundaries between α-phase grains and β-phase grains due to intercrystalline cavities. Their nucleation is thought to be heterogeneous at oxide or other particles, and their growth is attributed to vacancy condensation. Intercrystalline cavity formation induces a micro-void shear localization process and proceeds intercrystalline cracking.

It is valuable that the instability feature in the β-phase regime was also captured in the microstructures of deformed specimens. In Fig. 10(c) the microstructure under the unstable deforming condition of 1323 K (above β transus) & 10 s^{-1} shows that a long crack appears at the boundaries of coarse β-phase grains. The ξ-value under this condition is about -0.01, and m-value about 0.12. According to DMM theory, lower m-values, which mean fewer slip systems, mainly correspond with unstable regions with negative ξ-values. And the negative ξ-values usually correspond to these conditions that promote instabilities such as dynamic strain aging (DSA), adiabatic shear bands (ASB), flow localization bands or initiation and growth of microcracks.[31] The crack morphology shows the characteristics of micro-cracks initiation from micro-voids and its growth accelerated by the lack of non-basal slips.

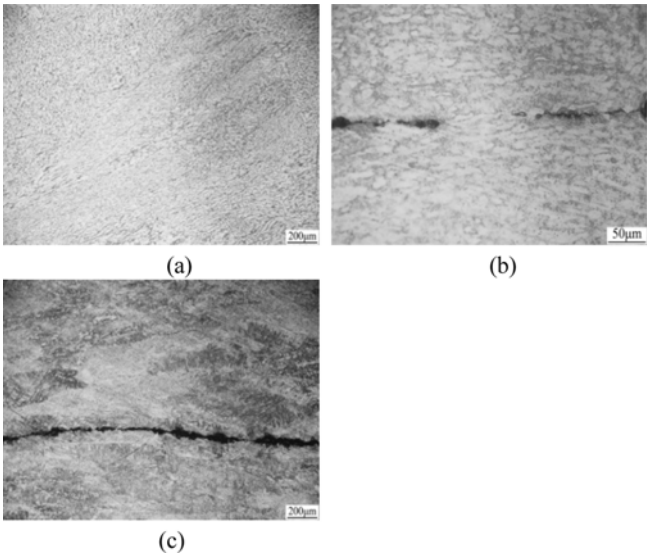

Fig. 10 The microstructures under the unstable deforming condition of (a) 1023 K & 1 s^{-1}; (b) 1173 K & 0.1 s^{-1}; (c) 1323 K & 10 s^{-1}

It is noted that DRV contributes to the restoration of micro-voids and even micro-cracks, while the DRV of β-phase is weakened under a higher strain rate, here 10 s^{-1}.

5. Conclusions

The hot deformation behaviors of Ti-6Al-4V alloy have been investigated in the temperature range of 1023~1323 K and the strain rate range of 0.01~10 s^{-1}. From isothermal compression data, the volume of strain-stress data was expanded by the BP-ANN model. Following which, the deformation active energy was calculated, the kinetics equation and processing maps were constructed. And the following important conclusions have been obtained:

1) A BP-ANN model was developed, and the correlation coefficients (R) and the average absolute relative error ($AARE$) of the BP-ANN model are 0.9999, 0.51% and 0.9998, 0.79% for α+β-phase field and single β-phase field, respectively, which indicates this model has desired precision and reliability.

2) The stress-strain curves of Ti-6Al-4V alloy are sensitive to temperature and strain rate. Generally, the stress decreases with the increasing temperature at a given strain rate and decreasing strain rate at a given temperature. In addition, the stress-strain curves indicate the intrinsic relationships between the flow stress and microstructural mechanisms in some degree.

3) The hot deformation apparent activation energy at the strain of 0.5 was calculated to be 564.05 kJ·mol^{-1} and 300.20 kJ·mol^{-1} for α+β-phase field and single β-phase field, respectively. The effect of deformation parameters (temperature and strain rate) on flow stress can be described by the following equations:

In the α+β-phase field,

$$\dot{\varepsilon} = 1.43 \times 10^{25} (\sinh(0.0061\sigma))^{4.70} \exp\left(\frac{-564.05}{RT}\right)$$

In single β-phase field,

$$\dot{\varepsilon} = 1.94 \times 10^{11} (\sinh(0.0235\sigma))^{3.36} \exp\left(\frac{-300.20}{RT}\right)$$

4) Based on the intensive stress-strain data, the processing maps of Ti-6Al-4V alloy at the strains of 0.3, 0.5, 0.7 and 0.9 were plotted by superimposing instability maps on power dissipation maps. From which, the stable and unstable regions were clarified clearly. And the optimum deformation conditions at the different strains are the temperature range of 1198 K~1248 K and strain rate range of 0.01-0.032s^{-1} for α+β-phase field and the temperature range of 1263-1323 K and strain rate range of 0.032~0.56 s^{-1} for single β-phase field, respectively.

5) The desired deformation mechanisms such as the globularization of α-phase in α+β-phase temperature range and the DRV of β-phase in β-phase temperature range were identified and validated by microstructure observations.

ACKNOWLEDGEMENT

This work was supported by National Natural Science Foundation of China (51305469).

REFERENCES

1. Peng, W., Zeng, W., Wang, Q., and Yu, H., "Comparative Study on Constitutive Relationship of AS-Cast Ti60 Titanium Alloy during Hot Deformation based on Arrhenius-Type and Artificial Neural Network Models," Materials & Design, Vol. 51, No. pp. 95-104, 2013.
2. Ning, Y., Fu, M. W., Hou, H., Yao, Z., and Guo, H., "Hot Deformation Behavior of Ti-5.0 Al-2.40 Sn-2.02 Zr-3.86 Mo-3.91 Cr Alloy with an Initial Lamellar Microstructure in the α+β Phase Field," Materials Science and Engineering: A, Vol. 528, No. 3, pp. 1812-1818, 2011.
3. Tan, Y. B., Duan, J. L., Yang, L. H., Liu, W. C., Zhang, J. W., and Liu, R. P., "Hot Deformation Behavior of Ti-20Zr-6.5 Al-4V Alloy in the α+β and Single β Phase Field," Materials Science and Engineering: A, Vol. 609, pp. 226-234, 2014.
4. Yadroitsev, I., Krakhmalev, P., and Yadroitsava, I., "Selective Laser Melting of Ti6Al4V Alloy for Biomedical Applications: Temperature Monitoring and Microstructural Evolution," Journal of Alloys and Compounds, Vol. 583, pp. 404-409, 2014.
5. Quan, G.-Z., Lv, W.-Q., Liang, J.-T., Pu, S.-A., Luo, G.-C., and Liu, Q., "Evaluation of the Hot Workability Corresponding to Complex Deformation Mechanism Evolution for Ti-10V-2Fe-3Al Alloy in a Wide Condition Range," Journal of Materials Processing Technology, Vol. 221, pp. 66-79, 2015.
6. Zhang, D.-Y., Li, H.-Z., Liang, X.-P., Wei, Z.-W., and Liu, Y., "Microstructure Characteristic for High Temperature Deformation of Powder Metallurgy Ti-47Al-2Cr-0.2Mo Alloy," Materials & Design, Vol. 59, pp. 415-420, 2014.
7. Ding, R., Guo, Z., and Wilson, A., "Microstructural Evolution of A Ti-6Al-4V Alloy during Thermomechanical Processing," Materials Science and Engineering: A, Vol. 327, No. 2, pp. 233-245, 2002.
8. Peng, X., Guo, H., Shi, Z., Qin, C., Zhao, Z., and Yao, Z., "Study on the Hot Deformation Behavior of TC4-DT Alloy with Equiaxed α+β Starting Structure based on Processing Map," Materials Science and Engineering: A, Vol. 605, pp. 80-88, 2014.
9. Reddy, N. S., Lee, Y. H., Park, C. H., and Lee, C. S., "Prediction of Flow Stress in Ti-6Al-4V Alloy with an Equiaxed α+β Microstructure by Artificial Neural Networks," Materials Science and Engineering: A, Vol. 492, No. 1, pp. 276-282, 2008.
10. Porntadawit, J., Uthaisangsuk, V., and Choungthong, P., "Modeling of Flow Behavior of Ti-6Al-4V Alloy at Elevated Temperatures," Materials Science and Engineering: A, Vol. 599, pp. 212-222, 2014.
11. Park, N.-K., Yeom, J.-T., and Na, Y.-S., "Characterization of Deformation Stability in Hot Forging of Conventional Ti-6Al-4V using Processing Maps," Journal of Materials Processing Technology, Vols. 130-131, pp. 540-545, 2002.
12. Seshacharyulu, T., Medeiros, S., Frazier, W., and Prasad, Y., "Microstructural Mechanisms during Hot Working of Commercial Grade Ti-6Al-4V with Lamellar Starting Structure," Materials Science and Engineering: A, Vol. 325, No. 1, pp. 112-125, 2002.
13. Reddy, N. S., Lee, Y.-H., Kim, J. H., and Lee, C. S., "High Temperature Deformation Behavior of Ti-6Al-4V Alloy with and Equiaxed Microstructure: A Neural Networks Analysis," Metals and Materials International, Vol. 14, No. 2, pp. 213-221, 2008.
14. Sun, Y., Zeng, W.-D., Zhao, Y.-Q., Zhang, X.-M., Ma, X., and Han, Y.-F., "Constructing Processing Map of Ti40 Alloy using Artificial Neural Network," Transactions of the Nonferrous Metals Society of China, Vol. 21, No. 1, pp. 159-165, 2011.
15. Wen, T., Yue, Y.-W., Liu, L.-T., and Yu, J.-M., "Evaluation and Prediction of Hot Rheological Properties of Ti-6Al-4V in Dual-Phase Region using Processing Map and Artificial Neural Network," Indian Journal of Engineering and Materials Sciences, Vol. 21, No. 6, pp. 647-656, 2014.
16. Zhao, J., Ding, H., Zhao, W., Huang, M., Wei, D., and Jiang, Z., "Modelling of the Hot Deformation Behaviour of a Titanium Alloy using Constitutive Equations and Artificial Neural Network," Computational Materials Science, Vol. 92, pp. 47-56, 2014.
17. Phaniraj, M. P. and Lahiri, A. K., "The Applicability of Neural Network Model to Predict Flow Stress for Carbon Steels," Journal of Materials Processing Technology, Vol. 141, No. 2, pp. 219-227, 2003.
18. Sun, Y., Zeng, W. D., Zhao, Y. Q., Zhang, X. M., Shu, Y., and Zhou, Y. G., "Modeling Constitutive Relationship of Ti40 Alloy using Artificial Neural Network," Materials & Design, Vol. 32, No. 3, pp. 1537-1541, 2011.

19. Sun, Y., Zeng, W. D., Zhao, Y. Q., Zhang, X. M., Shu, Y., and Zhou, Y. G., "Modeling Constitutive Relationship of Ti40 Alloy using Artificial Neural Network," Materials & Design, Vol. 32, No. 3, pp. 1537-1541, 2011.

20. Seshacharyulu, T., Medeiros, S. C., Frazier, W. G., and Prasad, Y. V. R. K., "Hot Working of Commercial Ti-6Al-4V with an Equiaxed α-β Microstructure: Materials Modeling Considerations," Materials Science and Engineering: A, Vol. 284, No. 1, pp. 184-194, 2000.

21. Prasad, Y., Gegel, H. L., Doraivelu, S. M., Malas, J. C., Morgan, J. T., et al., "Modeling of Dynamic Material Behavior in Hot Deformation: Forging of Ti-6242," Metallurgical Transactions A, Vol. 15, No. 10, pp. 1883-1892, 1984.

22. Quan, G.-Z., Ku, T.-W., Song, W.-J., and Kang, B.-S., "The Workability Evaluation of Wrought AZ80 Magnesium Alloy in Hot Compression," Materials & Design, Vol. 32, No. 4, pp. 2462-2468, 2011.

23. Quan, G.-Z., Liang, J.-T., Liu, Y.-Y., Luo, G.-C., and Zhou, J., "Identification of Optimal Deforming Parameters from a Large Range of Strain, Strain Rate and Temperature for 3Cr20Ni10W2 Heat-Resistant Alloy," Materials & Design, Vol. 52, pp. 593-601, 2013.

24. Quan, G.-Z., Wang, Y., Yu, C.-T., and Zhou, J., "Hot Workability Characteristics of AS-Cast Titanium Alloy Ti-6Al-2Zr-1Mo-1V: A Study using Processing Map," Materials Science and Engineering: A, Vol. 564, pp. 46-56, 2013.

25. Somani, M. C., Muraleedharan, K., Prasad, Y., and Singh, V., "Mechanical Processing and Microstructural Control in Hot Working of Hot Isostatically Pressed P/M in-100 Superalloy," Materials Science and Engineering: A, Vol. 245, No. 1, pp. 88-99, 1998.

26. Zhang, H., Zhang, K., Lu, Z., Zhao, C., and Yang, X., "Hot Deformation Behavior and Processing Map of a γ-Hardened Nickel-based Superalloy," Materials Science and Engineering: A, Vol. 604, pp. 1-8, 2014.

27. Zhao, H., Xiao, L., Ge, P., Sun, J., and Xi, Z., "Hot Deformation Behavior and Processing Maps of Ti-1300 Alloy," Materials Science and Engineering: A, Vol. 604, pp. 111-116, 2014.

28. Gegel, H. L., Malas, J. C., Prasad, Y. V., Doraivelu, S. M., Barker, D. R., et al., "Optimizing Hot Workability and Controlling Microstructures in Difficult to Process High Strength and High Temperature Materials," US Patent, No. 4617817 A, 1986.

29. Kim, J. S., Chang, Y. W., and Lee, C. S., "Mechanical and Microstructural Analysis on the Superplastic Deformation Behavior of Two-Phase Ti-6A1-4V Alloy," Metals and Materials, Vol. 4, No. 4, pp. 771-777, 1998.

30. Kim, J. S., Nam, W. J., and Lee, C. S., "Effect of Volume Fraction on the Dynamic Grain Growth during Superplastic Deformation of Ti3Al-based Alloys," Metals and Materials, Vol. 4, No. 5, pp. 1041-1046, 1998.

31. Quan, G.-z., Zhao, L., Chen, T., Wang, Y., Mao, Y.-p., Lv, W.-q., and Zhou, J., "Identification for the Optimal Working Parameters of AS-Extruded 42CrMo High-Strength Steel from a Large Range of Strain, Strain Rate and Temperature," Materials Science and Engineering: A, Vol. 538, pp. 364-373, 2012.